

Determining thermal dust emission from Planck HFI data using a sparse, parametric technique

Melis O. Irfan¹, Jérôme Bobin¹, and Marc-Antoine Miville-Deschénes¹

Laboratoire CosmoStat, AIM, UMR CEA-CNRS-Paris 7 Irfu, DAp/DEDIP, CEA Saclay, F-91191 GIF-SUR-YVETTE CEDEX, France.
 e-mail: melis.irfan@cea.fr

Received XXX XX, XXXX; accepted XXX XX, XXXX

ABSTRACT

Context. The *Planck* 2015 data release provided the community with high frequency ($\nu > 100$ GHz) observations of the full-sky at unprecedented resolutions. These maps contain a wealth of information on the cosmic microwave background (CMB), cosmic infrared background (CIB), extragalactic point sources and diffuse thermal dust emission.

Aims. We aim to determine the modified black body (MBB) model parameters of thermal dust emission and produce all sky maps of pure thermal dust, having separated this Galactic component from the CMB and CIB.

Methods. This separation is completed using a new, sparsity-based, parametric method which we refer to as *premise*. The method comprises of three main stages: 1) filtering of the raw data to reduce the effect of the CIB on the MBB fit. 2) fitting an MBB model to the filtered data across super-pixels of various sizes determined by the algorithm itself and 3) refining these super-pixel estimates into full resolution maps of the MBB parameters.

Results. We show

Conclusions. We believe...

Key words. Cosmology: Cosmic Microwave Background – ISM: dust, extinction – Methods: Data Analysis

1. Introduction

The meticulous separation of the cosmic microwave background (CMB) from astrophysical foregrounds is a pivotal step in extracting cosmological information from the *Planck* data. Several component separation techniques are currently in use; techniques such as SEVEM (Fernández-Cobos et al. 2012), NILC (Delabrouille et al. 2009), SMICA (Delabrouille et al. 2003) and L-GMCA (Bobin et al. 2014) are specialised to recover only the CMB signal from all other emission sources. At present only Commander-Ruler, a Bayesian parametric technique, can produce estimates of the CMB as well as the astrophysical foregrounds. Most recently, a generalised version of NILC, coined GNILC, has been applied to *Planck* HFI data to recover the thermal dust emission (Planck Collaboration et al. 2016c). As our interest lies in the recovery of astrophysical foregrounds as well as the CMB, we initially focus on the specific problem of acquiring pure thermal dust emission maps tackled by Commander-Ruler and GNILC.

Thermal dust emission is the dominant diffuse Galactic emission within *Planck* HFI data. Within the three highest HFI channels (353, 545, 857 GHz) the other non-negligible contributions to the total flux density are the CMB, the cosmic infrared background (CIB), extragalactic point sources and instrumental noise. Whilst the resolvable extragalactic point sources can be masked out, the unresolved extragalactic background emission that makes up the CIB requires a more global solution. The CIB makes two contributions to the total flux measured at a particular frequency: a constant additive offset level and variations around this mean level referred to as the CIB anisotropies (CIBA). Planck Collaboration et al. (2014) observed that the

constant additive offset level can be measured using correlations with H_I data. The CIBA can be approximated as Gaussian at *Planck* resolutions (Planck Collaboration et al. (2014); Planck Collaboration et al. (2016c)) but at scales smaller than a few arcminutes it traces structure formation at high redshifts (Béthermin et al. 2013).

Though not strictly a component separation problem, as there is only one well-defined diffuse emission source within an almost-Gaussian background, the *Planck* HFI data are an excellent testbed for techniques which aim to identify and characterise emission sources. In Irfan & Bobin (2017) we presented a new parametric technique which exploited the sparse nature of astrophysical emissions within the wavelet domain yet completed the model-fit within the pixel domain. Following the work of Planck Collaboration et al. (2014) and Planck Collaboration et al. (2016c) we chose to use the modified black body (MBB) thermal dust model due to its existing success in the literature and small number of parameters (temperature (T), spectral index (β) and optical depth at 353 GHz (τ_{353})):

$$x_\nu = \tau_{353} \times B(T, \nu) \times \left(\frac{\nu}{353 \text{ GHz}} \right)^\beta, \quad (1)$$

where ν represents frequency in GHz and $B()$ denotes the black-body function. It should be noted that the single spectral index MBB is not the only possible model, Meisner & Finkbeiner (2015) show that when considering frequencies both below and above 353 GHz the use of two spectral indices (one for low frequencies, one for high) yields an improvement in the fit. More physically motivated dust particle models are also under consideration (Jones et al. (2017); Guillet et al. (2017)), as are models which account for spectral deviations from the average MBB fit

along a line-of-sight using Taylor expansion (Chluba et al. 2017) or, in polarisation, measurements of the 3D magnetic structure of dust clouds (Tassis & Pavlidou (2015); Poh & Dodelson (2017)). The technique presented in Irfan & Bobin (2017), herein referred to as `premise`, is flexible to advances in the field in that the algorithm can be updated to work with different models. Currently, though, we utilise the MBB model.

1.1. Existing thermal dust estimates

Planck Collaboration et al. (2014) observe that smoothing helps reduce the impact of the CIBA on the MBB fit and so only produce their all-sky maps of dust temperature and 353 GHz optical depth at the full 5 arcmin resolution of the *Planck* HFI data, whilst their spectral index map is at 30 arcmin. The Planck Collaboration et al. (2014) thermal dust estimates can then be reconstructed using their MBB parameter maps. In place of global smoothing, GNILC (Planck Collaboration et al. 2016c) on the other hand, choose to smooth only in regions where the CIBA dominates over thermal dust emission. As they apply their filtering in the wavelet domain they can also choose to apply the greatest degree of smoothing at the angular scales which are most dominated by the CIBA. GNILC use estimates for the CIB, CMB and instrumental noise to inform their selection of which regions to smooth. After smoothing and recomposition back into the pixel domain they can fit the MBB model, or in fact any model, to determine thermal dust model parameters.

Commander-Ruler (Planck Collaboration et al. 2016a) present two 353 GHz thermal dust estimates, both determined from an MBB fit but to different data sets. One of the dust estimates is produced at $N_{\text{side}} = 256$ with a 1 degree FWHM from a combination of the *Planck* LFI data, WMAP (Bennett et al. 2013) and Haslam (Haslam et al. 1982) data. The second, at $N_{\text{side}} = 2048$ with a 7.5 arcmin FWHM, uses only the *Planck* HFI data (excluding the 100 GHz observations) and only fits for the thermal dust spectral index, setting the thermal dust temperature at each pixel to the values determined from the low frequency fit. As Commander-Ruler is a Bayesian method, the thermal dust fit makes use of priors: a Gaussian distribution with a mean of 1.55 and standard deviation of 0.1 for the spectral index and a Gaussian distribution with a mean of 23 K and standard deviation of 3 K for temperature.

Liu et al. (2017) compare the thermal dust estimates produced by Planck Collaboration et al. (2014), GNILC and Commander-Ruler (at $N_{\text{side}} = 256$) after all maps have been smoothed to a common resolution of two degrees. By computing the angular power spectra of the MBB parameters they identify a striking difference between the Planck Collaboration et al. (2014) and GNILC spectral index power spectra at small angular scales. Although different features are visible in all three temperature and spectral index maps, Liu et al. (2017) show that the histogram distributions for the Planck Collaboration et al. (2014) and GNILC parameters are far more similar to each other than the Commander-Ruler distributions.

An additional check of the MBB temperature and spectral index is their correlation. There may be a physical mechanism which produces an anti-correlation between T and β ; Ysard et al. (2015) generate dust SEDs with various grain parameters and from MBB fits to these pure dust SEDs they find that the variation of grain properties results in an anti-correlation of MBB temperature and spectral index. However it has also been demonstrated that the presence of noise biases the MBB fits to also produce such an anti-correlation (Shetty et al. 2009). Liu et al. (2017) reveal both negative and positive correlations across var-

Table 1. Bandpass response used for IRIS/SFD colour corrections

Wavelength (μm)	Relative response
65.0	0.000
70.0	0.010
75.0	0.113
80.0	0.306
85.0	0.505
90.0	0.695
95.0	0.824
100.0	0.947
105.0	0.939
110.0	1.000
115.0	0.631
120.0	0.319
125.0	0.195
130.0	0.106
135.0	0.053
140.0	0.010

ious regions of the sky for the Commander-Ruler temperature and spectral indices.

This paper is the empirical data accompaniment of Irfan & Bobin (2017); we use `premise` to determine the thermal dust MBB parameters from *Planck*, second data release (PR2), HFI data. In section 2 we present the data used for our analysis, section 3 gives an overview of the `premise` method and section 4 presents our results.

2. Data

2.1. Total flux maps

We determine the thermal dust MBB parameters by fitting to total flux data at 353, 545, 857 and 3000 GHz. The *Planck* PR2 data release provides the 353, 545 and 857 GHz observations across the full sky at $N_{\text{side}} = 2048$ and with a FWHM of 5 arcmin. We make use of the total flux density estimate at 3000 GHz provided by Planck Collaboration et al. (2014). This map is a combination of the IRIS 3000 GHz map (Miville-Deschénes & Lagache 2005) and the SDF (Schlegel et al. 1998) 3000 GHz map which favours the SDF representation at scales larger than 30 arcmin and the IRIS representation at scales smaller than 30 arcmin, up to the 5 arcmin resolution of the IRIS map. We use the version of the combined IRIS and SDF map on the Planck Legacy Archive¹ which has had the point sources removed and inpainted.

Technically I have also removed the CMB dipole but I am not describing that as I shouldn't have to do that for PR3 data

2.1.1. Colour corrections

In order to account for the change of flux across the instrumental bandpasses, colour corrections have been calculated for the empirical data. For the 353, 545 and 857 GHz colour corrections the *Planck* HFI bandpasses have been used, while for the IRIS/SFD map the band response in Table 1 was used (need to say where this came from). As the colour corrections depend on the thermal dust temperature and spectral index they are calculated for each temperature and spectral index estimate within the model fitting routine.

¹ <http://pla.esac.esa.int/pla>

2.2. Simulated CIB and instrumental noise

The `premise` method employs a similar filtering technique to that of GNILC and so requires estimates of the CIB and instrumental noise. We use the FFP8 (Planck Collaboration et al. 2016b) simulations for the *Planck* HFI instrumental noise. Gaussian noise with a median level of 0.06 MJy sr^{-1} (Planck Collaboration et al. 2014) was used for the 3000 GHz instrumental noise map.

We also use the FFP8 estimates for the CIB at 353, 545 and 857 GHz but we alter their mean values to match the CIB offsets measured by GNILC: CIB estimate - mean value + GNILC offset value. The GNILC CIB offset values are 0.1248, 0.3356, 0.5561 MJy/sr for 353, 545 and 857 GHz, respectively (Planck Collaboration et al. 2016c). A 3000 GHz CIBA map of $N_{\text{side}} = 2048$ and FWHM 5 arcmin was created using the methodology detailed in Appendix C of Planck Collaboration et al. (2014). We then fix the CIB offset value of this map to the GNILC calculated value of 0.1128 MJy/sr in the same way as described for the HFI frequencies.

2.3. CMB

The `premise` method for estimating thermal dust requires for the total flux maps to have had the CMB removed. For this we use the CMB estimate of Bobin et al. (2016).

2.4. Additional data

We make use of the HI 4-PI Survey data (HI4PI Collaboration et al. 2016) to assess the accuracy of our thermal dust estimates (section 4)². These data are available as all-sky HEALPix maps (Górski et al. 2005) at $N_{\text{side}} = 1024$ and a FWHM of ~ 16.2 arcmin.

We also utilise the SDSS tenth data release quasar catalogue (Pâris et al. 2014) as well as the Green et al. (2018) map of interstellar reddening³ to access the accuracy of our optical depth at 353 GHz estimate.

(Green et al. 2018) provide $E(r_{p1} - z_{p1})$ measurements across 75 per cent of the sky; $E(r_{p1} - z_{p1}) \equiv E(\text{B-V})$ for $R_V \sim 3.1$. The map is based on stellar observations from Pan-STARRS1 (Chambers et al. 2016) and 2MASS (Skrutskie et al. 2006) data.

3. Method

The motivation behind `premise` is the wealth of astrophysical information now available; we choose to make use of astrophysical models for the foreground components aiming to accurately determine these model parameters. `premise` is a sparsity driven methodology (Parameter Recovery Exploiting Model Informed Sparse Estimates) and although the data are fit in the pixel domain, the filtering and parameter refinement steps take advantage of the sparse nature of thermal dust emission within the wavelet domain. In this section we recap the `premise` method and detail the preprocessing steps specific to determining thermal dust emission from *Planck* HFI data. We encourage the interested reader to consult Irfan & Bobin (2017) for the mathematical derivation of the `premise` algorithm.

`premise` has three main steps:

- first we filter the data to suppress the CIB and instrumental noise. We employ the GNILC technique of using a covariance matrix formed from CIB and instrumental noise

estimates but add to this method by exploiting the sparsity of thermal dust emission in the wavelet domain.

- then we avoid the computational cost of completing a pixel-by-pixel MBB fit by fitting to super-pixels. The unique aspect of this step being that the super-pixel areas are selected by the `premise` algorithm itself to ensure that the regions with the weakest signal-to-noise ratios are given the largest areas to average over.
- lastly we determine the optimum parameter values per original resolution pixel. Using the super-pixel, parameter maps as initial guesses we evoke a gradient descent at each pixel to minimise the least squares estimator. Once the gradient descent converges, we threshold the parameters in the wavelet domain to prevent non-sparse, noise terms from contributing to the final parameter estimates.

3.1. Pre-processing

We assume the CMB contribution at 3000 GHz to be negligible and so only subtract the Bobin et al. (2016) estimate of the CMB from the 353, 545 and 857 GHz data.

The raw data are in the form of HEALPix maps; the filtering and super-pixel fit steps of the algorithm are completed twelve times on each of the 2D HEALPix face.

3.2. Filtering

To suppress the impact of the CIBA on determining the MBB parameters, `premise` employs a modified version of the GNILC filtering technique on the CMB subtracted data. GNILC use smoothing to suppress the CIBA within the regions of the total flux maps, at each scale within the spherical wavelet domain, where the nuisance (non-thermal dust) contributions dominate over the thermal dust signal. This technique relies upon the assumption that both the instrumental noise and CIB can be approximated as Gaussian.

For `premise` we apply the GNILC filtering as follows for each wavelet scale (j):

1. We define the nuisance term as $\mathbf{N} = \text{CIB estimate} + \text{instrumental noise estimate}$.
2. The raw data and nuisance estimates are divided into overlapping super-pixels of area 8×8 with an overlapping ratio of 0.5. We differ from GNILC in this respect as they choose instead to smooth the data and nuisance estimates.
3. The \mathbf{N}_{obs} by \mathbf{N}_{obs} nuisance covariance matrix is calculated as:

$$\mathbf{R}_{\text{nus}} = \frac{1}{N_{\text{pix}}} (\mathbf{N} \times \mathbf{N}^T) \quad (2)$$

4. The covariance matrices of the binned total flux maps were calculated for each bin: $\mathbf{R}_{\text{tot}} = \frac{1}{\text{bin area}} \mathbf{X} \times \mathbf{X}^T$ and then whitened: $\mathbf{R}_{\text{nus}}^{-1/2} \mathbf{R}_{\text{tot}} \mathbf{R}_{\text{nus}}^{-1/2}$.
5. The eigenvectors of the whitened \mathbf{R}_{tot} is calculated for each bin and ordered.
6. The Marcenko-Pastur distribution is used to select eigenvalues which deviate significantly from unity. Here we again differ from GNILC, who use the Akaike Information

² <https://lambda.gsfc.nasa.gov>

³ <http://argonaut.skymaps.info>

Criterion to select the eigenvalues which represent the signal sub-space.

7. The selected eigenvectors (\mathbf{U}_s) give the mixing matrix ($\mathbf{F} = \mathbf{R}_{\text{nus}}^{1/2} \mathbf{U}_s$) which can be used to obtain the least-squares optimisation of thermal dust emission. We, however choose to add a additional factor to the optimisation performed by GNILC. We recapture thermal dust information lost through binning by adding a penalisation factor to favour sparsity into the least-squares minimisation.
8. It should be noted that a user-defined threshold value is required to identify significant wavelet coefficients, i.e. those which are high enough above the noise level to be considered signal.

Our filtering uses two wavelet scales and a threshold cut-off value of 2.4.

3.3. Large-scale CIB offset and point sources

After filtering to deal with the CIBA and instrumental noise we need to remove the large-scale CIB offset before we can fit the MBB model. To enable a direct comparison between our results and that of GNILC we simply use the CIB offsets given in [Planck Collaboration et al. \(2016c\)](#): 0.1248, 0.3356, 0.5561 and 0.1128 MJy/sr for 353, 545, 857 and 3000 GHz, respectively.

The 3000 GHz total flux we use has already had its point sources masked and inpainted ([Planck Collaboration et al. 2014](#)) so we only need to mask the 353, 545 and 857 GHz data. For this we use the 2015 *Planck* HFI point source masks.

3.4. Super-pixel fit

We perform our MBB super-pixel fit on the filtered, large-scale CIB offset removed, point source masked data. The fit works on each of the twelve 2048X2048, HEALPix 2D faces as follows:

1. The instrumental noise + CIB covariance matrix is calculated for the full face within the wavelet domain for four wavelet scales.
2. The 2048X2048 face is split into patches of 128X128.
3. An MBB is fit to each 128X128 patch.
4. The data-model residual within each patch is calculated per original pixel and transformed into the wavelet domain, again using four wavelet scales.
5. The reduced χ^2 at each of the four wavelet scales is calculated for each pixel.
6. The data are split into super-pixels according to the reduced χ^2 ; if more than ten per cent of the pixels in a 64X64 patch contain reduced χ^2 values greater than 2 within the third wavelet scale then the patch is split into four 32X32 patches. If more than ten per cent of the pixels in a 32X32 patch contain reduced χ^2 values greater than 2 within the second wavelet scale then the patch is split into four 16X16 patches and so on.
7. A lower limit of 8X8 patches is enforced and the algorithm is also prevented from cutting up the data into patch sizes which only contained masked data.

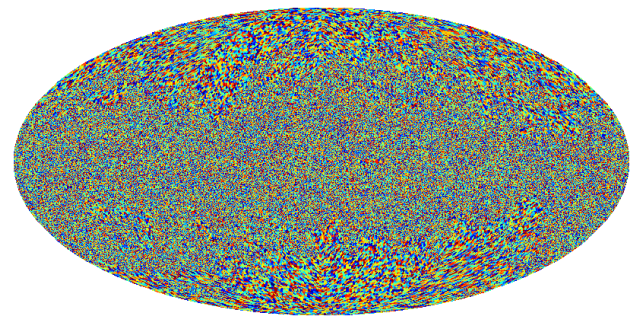


Fig. 1. All-sky map of premise super-pixels. Colour scale represents the random numbers used to highlight the different pixels areas.

8. The MBB fit is then re-run fit on the algorithm chosen super-pixels to obtain initial parameter estimates. Fig. 1 shows the super-pixels chosen.

3.5. Refinement

The refinement step of the premise algorithm is the final step and provides us with all-sky, full resolution maps of the MBB parameters. As the three MBB parameters suffer from degeneracies we shall first only discuss temperature and spectral index and then attempt to break the degeneracy, with additional data, to determine the optical depth at 353 GHz.

3.5.1. Temperature and Spectral Index

The super-pixel fit produces initial estimates of the MBB temperature and spectral index. As these initial estimates are well informed we can use them to seed a gradient descent algorithm to determine the optimum temperature and spectral index per pixel. First we use the initial temperature estimate (T^0) to provide an initial optical depth estimate from the 353 GHz empirical measurement: $\tau_{353}^0 = X_{353}/B(T^0, 353 \text{ GHz})$. We can then construct a thermal dust model at each frequency (ν) as $\tau_{353}^0 \times B(T^0, \nu) \times (\nu/353)^{\beta^0}$. The gradient descent is performed iteratively, per pixel, for both temperature and spectral index as follows:

$$\beta/T^{(t+1)} = \beta/T^{(t)} + \alpha \left(\frac{\partial X}{\partial \beta/T} \right)^T \text{Model} \times (X - \text{Model}). \quad (3)$$

The gradient path length (α) is computed analytically at each iteration; it is the minimum of the inverse Hessian matrix of the data-model residual (with respect to β and T). The gradient descent is terminated upon convergence, which we define as the point when two iterations only differ in their parameter estimation by less than 10^{-6} .

After the gradient descent step we now have two all-sky maps, one of temperature and one of spectral index. These maps are at the full *Planck* resolutions of 5 arcmin as the gradient descent step uses the empirical data, not the filtered data from section 3.2. Using the spherical wavelet transform we soft threshold these maps in the wavelet domain (leaving the coarse scale untouched) to remove the effect of any non-sparse elements in the total flux maps. The threshold values are calculated at each of the five wavelet scales as double the mean absolute deviation (MAD) of the temperature/spectral index. As variance cannot be calculated per pixel we divide the data into patches of 32X32 pixels

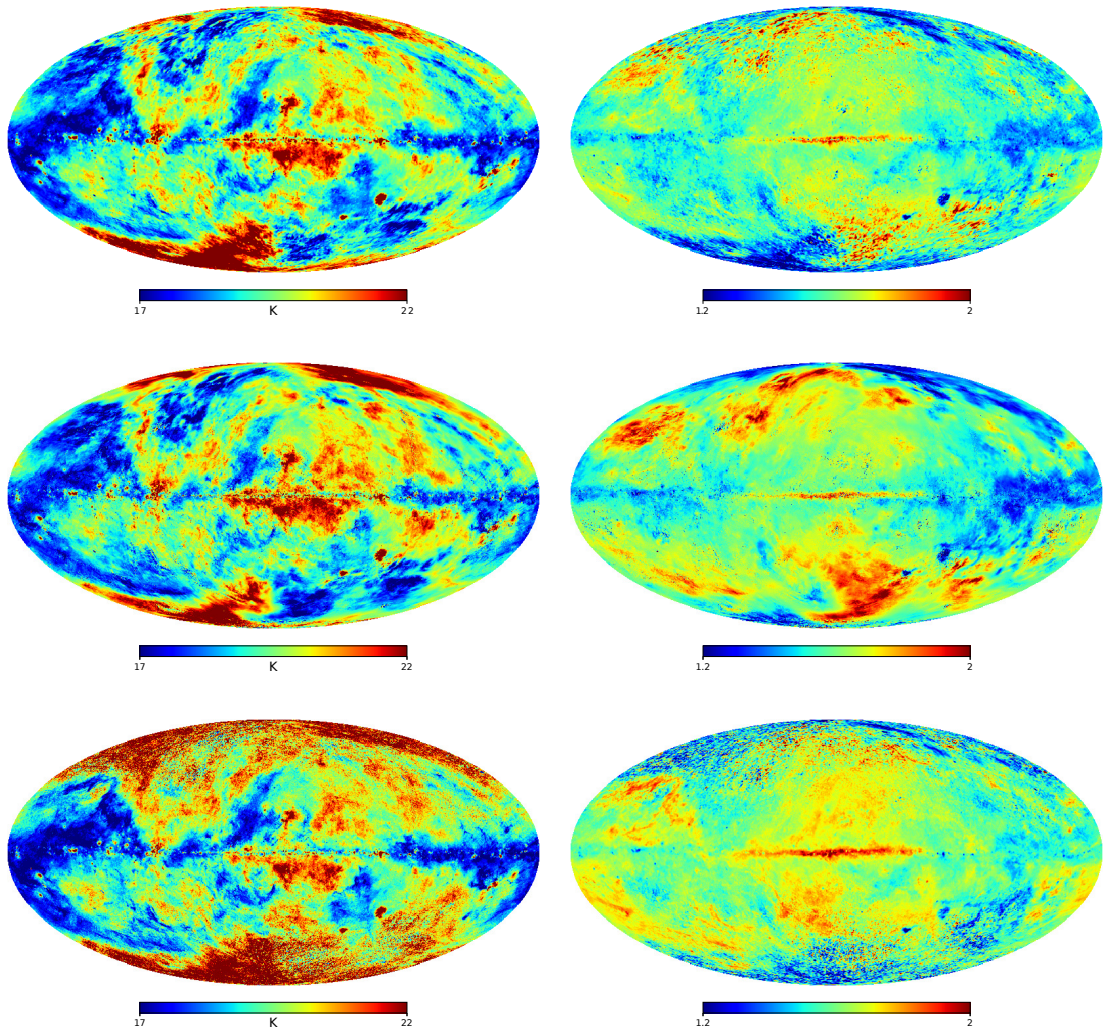


Fig. 2. Thermal dust MBB temperatures (*left*) and spectral indices (*right*) as calculated by `premise` (*top*), `GNILC` (*middle*) and `2013` (*bottom*).

for the MAD calculation. Thresholding removes non-sparse information from the wavelet scales and so if, for a particular region and angular scale, the signal is completely subdominant to the noise then we loose the signal for that region at that resolution.

As long as the Shannon sampling condition is obeyed, the wavelet transform does not require information at each map pixel in order to reconstruct the all-sky maps. As opposed to the gradient descent step, which does require complete information at each pixel. Therefore we can re-apply the *Planck* HFI masks at each frequency before thresholding in the wavelet domain in order to prevent the point sources from contributing the final temperature and spectral index estimates. The process of gradient descent followed by thresholding within the wavelet domain is then repeated to ensure a robust solution.

3.5.2. Optical depth at 353 GHz

The MBB parameters are heavily degenerate when fit in the presence of CIB and noise. Both [Planck Collaboration et al. \(2014\)](#) and [Planck Collaboration et al. \(2016c\)](#) try to combat this degeneracy through smoothing. The `premise` super-pixel MBB fit is specialised to select super-pixels sizes based on the spatial variation of the dust temperature and spectral index, as of such the

same method is less responsive to the overall normalisation factor (the optical depth).

To break the parameter degeneracies we return to the empirical data set for additional information: the 3000 GHz IRIS+SDF map, which has the lowest CIB contamination out of the empirical data set. We calculate the optical depth at 5 arcmin using the IRIS+SFD total flux map and the `premise` estimates for temperature and spectral index:

$$\tau_{353} = \frac{(x_{3000} - c_{3000}) \times cc}{B(T, 3000 \text{ GHz}) \times \left(\frac{3000 \text{ GHz}}{353 \text{ GHz}}\right)^\beta}, \quad (4)$$

where c_{3000} is the large-scale CIB offset for the IRIS/SFD map and cc is the colour correction for the COBE/DIRBE bandpass. The IRIS/SFD map has already had its point sources inpainted so no further processing of this map is required.

4. Results

We aim to assess our thermal dust MBB parameters through comparisons with existing thermal dust templates and external data sets. Within this section we shall refer to the results obtained by [Planck Collaboration et al. \(2014\)](#) as 2013 (*I will think of a better name*).

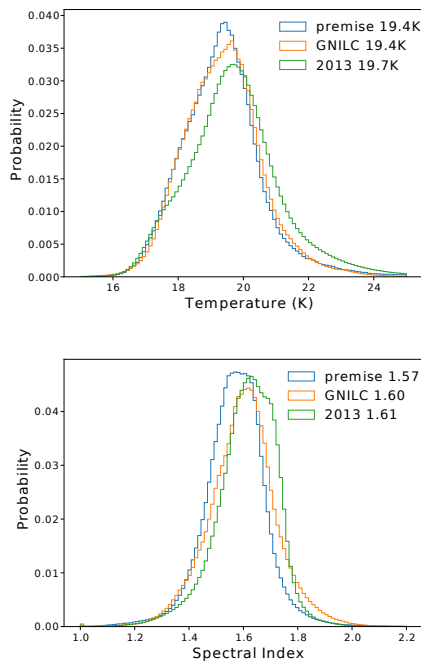


Fig. 3. Histogram comparison between premise, 2013 and GNILC temperatures (top) and spectral indices (bottom).

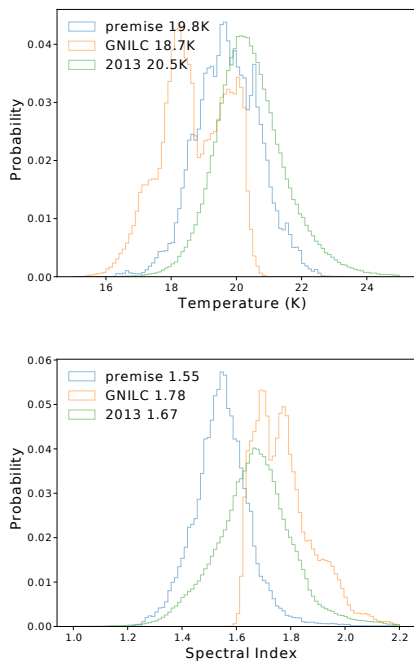


Fig. 4. Histogram comparison between premise, 2013 and GNILC temperatures (top) and spectral indices (bottom) within $l = 5^\circ - 65^\circ$ and $b = 58^\circ - 78^\circ$.

4.1. Temperature and Spectral Index: spatial distributions

Fig. 2 shows the all-sky MBB temperature and spectral index for thermal dust emission as calculated by premise, 2013 and GNILC. Visually, the premise and GNILC temperature maps look most similar, differing from the 2013 temperature maps noticeably at high latitudes. Interestingly, for spectral index the premise map resembles the GNILC result within the southern

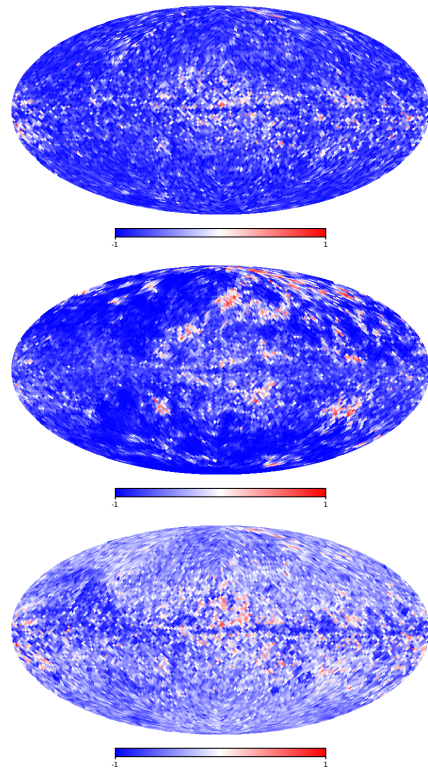


Fig. 5. Temperature and spectral index correlation maps for premise parameters (top), GNILC parameters (middle) and 2013 parameters (bottom). The colour scale represents the correlation coefficient values.

hemisphere and the 2013 result within the northern hemisphere. Fig. 3 shows the temperature and spectral index normalised distributions for the three estimates as histograms (100 bins). The mean spectral index and temperature values are 19.4 K and 1.57 respectively for premise, 19.4 K and 1.60 respectively for GNILC and 19.7 K and 1.61 for 2013.

To further probe the discrepancies in spectral index at high Galactic latitudes we now consider only pixels within the Galactic longitude range of $5^\circ - 65^\circ$ and latitude range of $58^\circ - 78^\circ$. The histograms in Fig. 4 show the distributions of the temperatures and spectral indices within this region as calculated by premise, 2013 and GNILC; the premise values have a mean of 1.55 and 19.8 K for spectral index and temperature, respectively while the GNILC mean values are 1.78 and 18.7 K and the 2013 mean values within this region are 1.67 and 20.5 K.

4.2. Temperature and Spectral Index: anti-correlations

A possible check of MBB temperature and spectral index is their correlation. While it may be possible for there to be a physical mechanism which produces an anti-correlation between T and β , it is known that the presence of noise biases the MBB fits to also produce such an anti-correlation (Shetty et al. 2009).

Fig. 5 shows correlation coefficient maps made by dividing the full sky into patches of 64X64 pixels, giving just under two degrees of resolution. Each patch is coloured according to the correlation coefficient determined for the 4096 pixels within the area. Larger patches of correlated and anti-correlated pixels appear at high latitudes (low signal to noise regions) for GNILC than for premise. The 2013 temperature and spectral index values can be seen to be barely correlated.

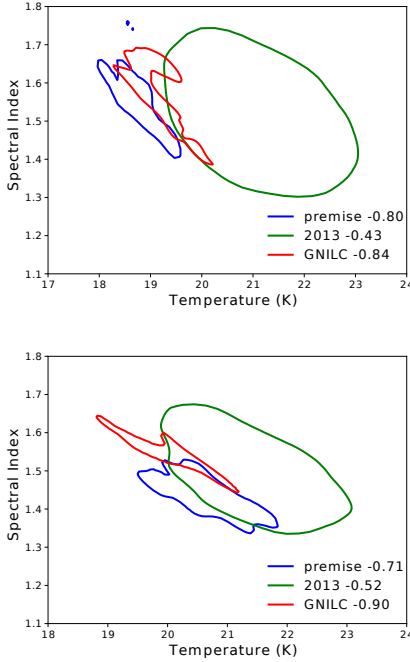


Fig. 6. Contour plots of temperature and spectral index for *premise*, GNILC and 2013. The one sigma level contour is shown for a five degree radius circle of pixels centred at $(l, b) = (90^\circ, 80^\circ)$ (*top*) and $(l, b) = (270^\circ, -80^\circ)$ (*bottom*).

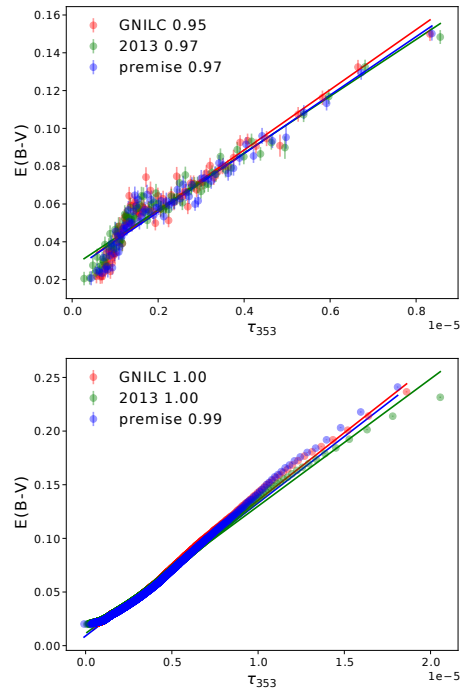


Fig. 7. Linear relationship between $E(B-V)$ and optical depth at 353 GHz for *premise*, GNILC and 2013. $E(B-V)$ values have been calculated using the SDSS quasars (*top*)/Green reddening map (*bottom*).

Table 2. Linear regression parameters: SDSS reddening vs. τ_{353}

Method	Gradient	Intercept
2013	$(1.50 \pm 0.05)10^4$	$(27 \pm 1)10^{-3}$
<i>premise</i>	$(1.55 \pm 0.05)10^4$	$(25 \pm 1)10^{-3}$
GNILC	$(1.59 \pm 0.06)10^4$	$(25 \pm 2)10^{-3}$

Table 3. Linear regression parameters: Green reddening map vs. τ_{353}

Method	Gradient	Intercept
2013	$(1.19 \pm 0.003)10^4$	$(11.4 \pm 0.08)10^{-3}$
<i>premise</i>	$(1.24 \pm 0.003)10^4$	$(9.0 \pm 0.10)10^{-3}$
GNILC	$(1.26 \pm 0.002)10^4$	$(9.0 \pm 0.08)10^{-3}$

In Fig. 6 we take two particularly low signal-to-noise regions and examine the $T\text{-}\beta$ anti-correlation in the form of contour plots. The regions are both circles of radius five degrees, the first centred at $(l, b) = (90^\circ, 80^\circ)$, the second at $(l, b) = (270^\circ, -80^\circ)$. The pixels are binned and the one sigma contour levels are plotted. The correlation coefficients for the pixels within each regions are given on each plot. Again we see the lowest level of anti-correlation in both regions for the 2013 values and the highest for GNILC. Although smoothing helps to break the degeneracies introduced by the CIBA and instrumental noise, it may also suppress any actual, small-scale variations in the MBB parameters. The 2013 $T\text{-}\beta$ values occupy a larger parameter space indicating noisier measurements which, as each patch correlation coefficient is inversely proportional to the standard deviation of the $T\text{-}\beta$ values, results in lower coefficient magnitudes.

4.3. Optical depth at 353 GHz

The reddening of point source emission due to scattering within the interstellar-medium makes extinction measurements, $E(B-V)$, a valuable and independent check on thermal dust estimates. [Planck Collaboration et al. \(2014\)](#) make use of the SDSS quasar catalogue to determine correlations between $E(B-V)$ and τ_{353} , we replicate this analysis as detailed in section 6.1 and appendix E of their paper. In their analysis [Planck Collaboration et al. \(2014\)](#) use the seventh data release quasar catalogue whilst in our analysis we use the tenth data release ([Pâris et al. 2014](#)), resulting in 77291 quasars within the redshift range of $0.7 < z < 1.7$. Since the [Planck Collaboration et al. \(2014\)](#) analysis took place, a map of interstellar reddening ([Green et al. 2018](#)) has been made available; we make use of it and refer to it from herein as the Green reddening map.

Fig. 7 presents the linear relationship between τ_{353} and $E(B-V)$ for optical depth values calculated by *premise*, GNILC and 2013. The extinction values are binned according to optical depth values in bins of 1,000 for the top plot and in bins of 10,000 for the bottom plot. For the Green reddening map we choose to mask out the data across the Galactic plane using the *Planck* HFI Galactic plane 60 per cent mask without apodization.

The upper plot in Fig. 7 displays larger error bars than the bottom plot as the error bars are the standard deviation within the bin divided by the square root of the bin number; the Green reddening map bin size is a thousand times greater than the SDSS bin size. The correlation coefficients for the binned data are given on the plots and are seen to be strong between all three optical depth estimates and the $E(B-V)$ values from both SDSS and the Green reddening map. Table 2 and 3 show the linear fit parameters and their errors. For both the SDSS and Green reddening values the *premise* and 2013 linear fits posses more similar gradients to each other than to the GNILC fit. The fact

that `premise` and GNILC have identical y-intercept values because `premise` uses the GNILC values for the CIB large-scale offsets so the maps should share a common zero level.

As the correlations between optical depth estimates and interstellar reddening are indistinguishably strong for all three optical depth estimates, we now extend this analysis to thermal dust radiance estimates.

References

- Bennett, C. L., Larson, D., Weiland, J. L., et al. 2013, ApJS, 208, 20
 Béthermin, M., Wang, L., Doré, O., et al. 2013, A&A, 557, A66
 Bobin, J., Sureau, F., & Starck, J.-L. 2016, A&A, 591, A50
 Bobin, J., Sureau, F., Starck, J.-L., Rassat, A., & Paykari, P. 2014, A&A, 563, A105
 Chambers, K. C., Magnier, E. A., Metcalfe, N., et al. 2016, ArXiv e-prints [arXiv:1612.05560]
 Chluba, J., Hill, J. C., & Abitbol, M. H. 2017, MNRAS, 472, 1195
 Delabrouille, J., Cardoso, J.-F., Le Jeune, M., et al. 2009, A&A, 493, 835
 Delabrouille, J., Cardoso, J.-F., & Patanchon, G. 2003, MNRAS, 346, 1089
 Fernández-Cobos, R., Vielva, P., Barreiro, R. B., & Martínez-González, E. 2012, MNRAS, 420, 2162
 Górski, K. M., Hivon, E., Banday, A. J., et al. 2005, ApJ, 622, 759
 Green, G. M., Schlaflly, E. F., Finkbeiner, D., et al. 2018, ArXiv e-prints [arXiv:1801.03555]
 Guillet, V., Fanciullo, L., Verstraete, L., et al. 2017, ArXiv e-prints [arXiv:1710.04598]
 Haslam, C. G. T., Salter, C. J., Stoffel, H., & Wilson, W. E. 1982, A&AS, 47, 1
 HI4PI Collaboration, Ben Bekhti, N., Flöer, L., et al. 2016, A&A, 594, A116
 Irfan, M. & Bobin, J. 2017, ArXiv e-prints [arXiv:1711.10848]
 Jones, A. P., Köhler, M., Ysard, N., Bocchio, M., & Verstraete, L. 2017, A&A, 602, A46
 Liu, H., von Hausegger, S., & Naselsky, P. 2017, Phys. Rev. D, 95, 103517
 Meisner, A. M. & Finkbeiner, D. P. 2015, ApJ, 798, 88
 Miville-Deschénes, M.-A. & Lagache, G. 2005, ApJS, 157, 302
 Pâris, I., Petitjean, P., Aubourg, É., et al. 2014, A&A, 563, A54
 Planck Collaboration, Abergel, A., Ade, P. A. R., et al. 2014, A&A, 571, A11
 Planck Collaboration, Adam, R., Ade, P. A. R., et al. 2016a, A&A, 594, A10
 Planck Collaboration, Ade, P. A. R., Aghanim, N., et al. 2016b, A&A, 594, A12
 Planck Collaboration, Aghanim, N., Ashdown, M., et al. 2016c, A&A, 596, A109
 Poh, J. & Dodelson, S. 2017, Phys. Rev. D, 95, 103511
 Schlegel, D. J., Finkbeiner, D. P., & Davis, M. 1998, ApJ, 500, 525
 Shetty, R., Kauffmann, J., Schnee, S., & Goodman, A. A. 2009, ApJ, 696, 676
 Skrutskie, M. F., Cutri, R. M., Stiening, R., et al. 2006, AJ, 131, 1163
 Tassis, K. & Pavlidou, V. 2015, MNRAS, 451, L90
 Ysard, N., Köhler, M., Jones, A., et al. 2015, A&A, 577, A110